Carbohydrate Polymers 345 (2024) 122558

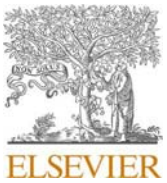

Contents lists available at ScienceDirect

Carbohydrate Polymers

journal homepage: www.elsevier.com/locate/carbpol

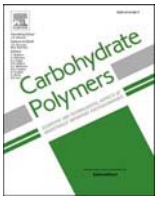

Janus nanocellulose membrane by nitrogen plasma: Hydrophilicity to hydrophobicity selective switch

Ana Oberlintner [a,*], Vasyl Shvalya [b], Neelakandan M. Santhosh [b], Martin Košiček [b], Ivan Jerman [c], Matej Huš [a,d,e], Uroš Cvelbar [b], Uroš Novak [a,*], Blaž Likozar [a]

[a] Department of Catalysis and Chemical Reaction Engineering, National Institute of Chemistry, Hajdrihova 19, SI-1000 Ljubljana, Slovenia
[b] Department of Gaseous Electronics, Institute Jožef Stefan, Jamova 39, SI-1000 Ljubljana, Slovenia
[c] Laboratory for Coating Development, Department of Materials Chemistry, National Institute of Chemistry, Hajdrihova 19, SI-1000 Ljubljana, Slovenia
[d] Association for Technical Culture of Slovenia (ZOTKS), Zaloška 65, SI-1000 Ljubljana, Slovenia
[e] Institute for the Protection of Cultural Heritage of Slovenia (ZVKDS), Poljanska 40, SI-1000 Ljubljana, Slovenia

ARTICLE INFO

Keywords:
Cellulose nanofibrils
Janus material
Nitrogen plasma modification
Surface hydrophobization
Wound dressing

ABSTRACT

Cellulose nanofibrils are one of the keystone materials for sustainable future, yet their poor water repellency hinders their push into industrial applications. Due to complexity and poor economical outcome and/or processing toxicity of the existing hydrophobization methods, nanocellulose loses against its antagonist plastic in medical and food industries. Herein, we demonstrate for the first time the "one-side selective water-repellency activation" in nanocellulose membranes by the means of mild N_2-plasma treatment, exhibiting lowest wettability after 20 s of treatment. Hydrophobicity and accompanying Janus character were justified by the topological, chemical and structural reorganizations in cellulose nanofibrils. The findings suggest that the mechanism behind the hydrophilic/hydrophobic change primarily relies on the interplay between OH removal and appearance of Si—CH_3, originating from the polysiloxanes-based substrate, as well as complementary C—NH_2 groups formation. First-principles calculations show that NH_2 groups moderately increase hydrophobicity, while various —Si—CH_3 substitutions wholly change the character of the surface to repel water. Using nitrogen is shown to be crucial, as —N(H)—Si—$(CH_3)_3$ groups induce greater hydrophobicity than simple O—Si—$(CH_3)_3$. Finally, the obtained materials absorb water on the hydrophilic side, while remaining hydrophobic on the other, exhibit high tensile strength, and protection against UV light, demonstrating applicability over wide range of applications.

1. Introduction

In light of ever-increasing demand for resources, turning away from society's high dependence on fossil-fuel based materials is unavoidable to warrant a sustainable future, pushing bio-based and bio-degradable materials into the spotlight. The abundance, versatility, biocompatibility and biodegradability of cellulose, calls for its wider utilization (Habibi & Lucia, 2012; Thomas et al., 2018). Regardless of the field of use, the native physicochemical characteristics of a cellulose and its nanostructured derivatives often do not meet the advanced application criteria. Developing methods that enable selective and, crucially, controllable tailoring of their properties, namely mechanical, antimicrobial, barrier and/or wettability which are subjects the most in cellulose-related industry in cellulose-related industry. The latter is vital in advanced applications spanning from emulsion separation through packaging to (medical) textile materials (Li et al., 2019; Provin et al., 2021; Wang et al., 2021). Although extensive efforts to obtain a sustainable, fast, effective, durable and industrially viable approach to tailor wetting properties of cellulose nanomaterials have been carried out, development of such is anything but trivial.

Wetting behavior is controlled by two features of the material: its free surface energy (FSE) and topology. On a completely smooth surface, FSE governs wettability and four initial states are possible: hydrophilicity (water contact angle (WCA) $< 90°$), oleophilicity (oil contact angle (OCA) $< 90°$), hydrophobicity (WCA $\geq 90°$) and oleophobicity (OCA $\geq 90°$) (Wang et al., 2015). Still, observing nature, it has managed to produce materials, such as lotus leaves and duck feathers, that exhibit superhydrophobic (WCA $> 150°$) and self-cleaning properties, puzzling

* Corresponding authors.
E-mail addresses: ana.oberlintner@ki.si (A. Oberlintner), uros.novak@ki.si (U. Novak).

https://doi.org/10.1016/j.carbpol.2024.122558
Received 27 March 2024; Received in revised form 26 July 2024; Accepted 29 July 2024
Available online 2 August 2024

researchers until mid-20th century, until Cassie and Baxter (1944) emphasized the importance of (micro)structure on extreme hydrophobicity (Cassie & Baxter, 1944). Therefore, to artificially obtain a material with extreme wetting properties, namely superhydrophobicity (SHB), superhydrophilicity (SHL), superoleophilicity (SOL) and superoleophobicity (SOB), the surface should feature micro or even nanostructures (Wang et al., 2015). It is worth mentioning that typically, superhydrophobic and superhydrophilic solid surfaces in air correspond to superoleophilic and superolephobic surfaces in air and underwater, respectively (Zhu et al., 2014). Materials composed of cellulose nanocrystals (CNCs) or cellulose nanofibrils (CNFs) already exhibit nanoroughness, hence to decrease their wettability, lowering FSE is targeted through exploitation of functional groups with lower polarity than OH through adsorption of hydrophobic species or functionalization with small molecules or polymers that induce hydrophobic interactions (Oberlintner et al., 2021).

Composed of highly reactive excited atomic, molecular, ionic and radical species, plasma is seen as an attractive technology for ultrafast surface modification of materials. Plasma enables a targeted 'mild' (surface) or/and 'harsh' (bulk) tailoring of physicochemical properties aiming to improve crystallinity, adhesion (Hegemann et al., 2003; Liston et al., 1993), dyeability (Haji & Naebe, 2020), biocompatibility (Recek, 2019; Valence et al., 2013) or wettability (Lejeune et al., 2006) of the final material (Chu et al., 2002). Additionally, omitting the need for solvents decreases downstream separation process units, eliminates liquid discharge, and thus lowers the environmental and economic burden, offering a further advantage compared to conventional wet-chemistry based functionalization techniques (Yasuda & Matsuzawa, 2005). Attaching silicon and fluorine-containing species discharged from SiH_4, CF_4, C_4F_8, SF_6 or their mixtures (Kawano et al., 2022; Kurniawan et al., 2012; Matouk et al., 2020, 2021; Oberlintner, Shvalya, et al., 2022; Silva et al., 2016; Vaswani et al., 2005) exhibit extremely high efficiency, with the surfaces often exceeding even the superhydrophobic threshold (water contact angle $\geq 150°$). Yet, due to rising concerns about their environmental footprint and impact on human health (Dimitrakellis & Gogolides, 2018), prompting the search for safer and eco-friendly solutions. On the other hand, use of environmentally inert gases e.g. O_2, N_2, Ar or NH_3 for formation of plasma was shown to provide the opposite: it further enhances the wettability (Flynn et al., 2013; Kawano et al., 2022; Kurniawan et al., 2012; Kutová et al., 2021; Matouk et al., 2020; Pertile et al., 2010). It should be noted that ammonia is less desirable for plasma generation due to its toxicity and corrosivity (Kwak et al., 2019).

Named after a Roman god of transitions, time and duality, Janus materials exhibit dual wettability behavior without external stimulus such as pH, (UV) light or temperature. Potential fields of applications for such materials include oil/water separation (Abuhantash et al., 2023; Agaba et al., 2021; Li et al., 2024), fog collection (Cao et al., 2014), bubble aeration (Yang et al., 2016), smart wound dressings (Cheng et al., 2020; Koşak Söz et al., 2018; Xu et al., 2024), and smart textiles (Dai et al., 2019). Yet, although plasma provides particularly surface oriented modifications and could be exploited for production of Janus materials, such modifications are seldom reported. Currently known methods to assemble cellulose-based Janus materials include deposition of ZnO nanorods on the cellulose membrane on one side and MnO_2 nanowires on the other (Yue et al., 2018), in situ immobilization of Ag nanoparticles and hydrophobization with stearic acid (Lv et al., 2019), electrospinning cellulose diacetate (Wang et al., 2020), separately preparing hydrophilic and hydrophobic sides of the Janus sponge and crosslinking them at elevated temperatures (Agaba et al., 2021), electrospraying glycerol propoxylate triglycidyl ether/octadecylamine coating (Zhou et al., 2022) or vapor deposition of silane compounds (Fei et al., 2022).

Considering this, the hypothesis is of the study is that through a novel approach including utilization of silicone substrate and nitrogen plasma, CNFs-based membranes with Janus behavior can be prepared. Considering wettability is determined by surface chemistry and morphology, both were thoroughly studied to obtain an insight into the dual wettability character. Lastly, applicability of as-prepared membrane is demonstrated, with final use as wound dressing material in mind.

2. Materials and methods

2.1. Materials

CNFs Valida S (produced from bleached hardwood kraft pulp, unmodified, prepared by mechanical fibrillation, 3 wt% gel, M_w = 214,700 g mol^{-1}, 1 wt% lignin, 71 wt% cellulose and 28 wt% hemicellulose (analyzed as specified in the Supplementary information), viscosity (1.0 % at 20 °C) = 950 mPa s, pH (1.0 %) = 6.9, content of heavy metals (Pb) < 20 mg kg^{-1}, As <2 mg kg^{-1}, total bacteria count < 100 cfu g^{-1}, total mold and yeast < 100 cfu g^{-1}, surface charge up to 0.1 meq g^{-1}) were obtained from Sappi (Maastricht, Netherlands). Glycerol was purchased from Pharmachem (Ljubljana, Slovenia). Silicone substrate was obtained from Galicja – Art (Gorlice, Poland). Ultrapure water (18 MΩ) was used throughout the experiments.

2.2. Methods

2.2.1. Preparation of membranes

Valida S CNFs were diluted with water to reach final concentration of CNFs in water 1.2 wt%. Glycerol was added in amount of 30 wt% based on mass of biopolymer. The dispersion was stirred at 1000 rpm on a magnetic mixer overnight, to obtain a homogeneous mixture. To obtain various thickness of the membranes, the membrane-forming solution in amounts 0.21 g cm^{-2}, 0.42 g cm^{-2}, and 0.84 g cm^{-2} was casted to Petri dishes, padded with silicone substrate that was previously thoroughly washed with soap and water, omitting ethanol and acetone. The membranes were dried for 24 h in a ventilated oven (Kambič, Slovenia) at 40 °C. After drying, the membranes were then gently peeled off and treated with plasma immediately. The side that was in contact with the air during drying was labeled "S-I" and the side in contact with silicone substrate was referred as "S-II" (Fig. 1a).

2.2.2. Plasma treatment

The samples were placed onto the glass slide with S-II facing up and fixated on the edges by them covering the edges with pieces of glass slides on carbon tape. This measure was taken, so the sample would not move during the experiment when establishing vacuum conditions. Plasma treatments were carried out in an in-house constructed system (RF = 13.56 MHz, inductively coupled plasma), consisting of an 80 cm long Borax glass tube with inner diameter of 4 cm. The experiments were carried out under stable vacuum conditions (1 Pa) at various nitrogen flows 50–400 sccm and different times. The sample was placed in at different positions (before glow, center of a coil, afterglow discharge) and powers (50–500 W) to unveil optimal balance between functionalization and sample surface damage. After the treatment, the system was filled with argon to prevent with instant oxidation.

2.2.3. Membrane characterization

Water contact angle (WCA) on the membranes was evaluated with tensiometer Theta T200 (Biolab Scientific, Sweden). Static sessile drop method was applied with the droplet size was set to 3 μL with WCA evaluated 5 s after the deposition of the drop to the surface. For drop shape analysis, Young-Laplace model was used for calculation of the final WCA.

Insight into structural properties was obtained through ATR-FTIR Omega 3 (Perkin Elmer, USA) in range 4000 cm^{-1}–400 cm^{-1} with resolution of 4 cm^{-1} and accumulation of 16 scans. Each sample was scanned three times and the average is reported.

The morphology of the fabricated CNFs-based membranes was

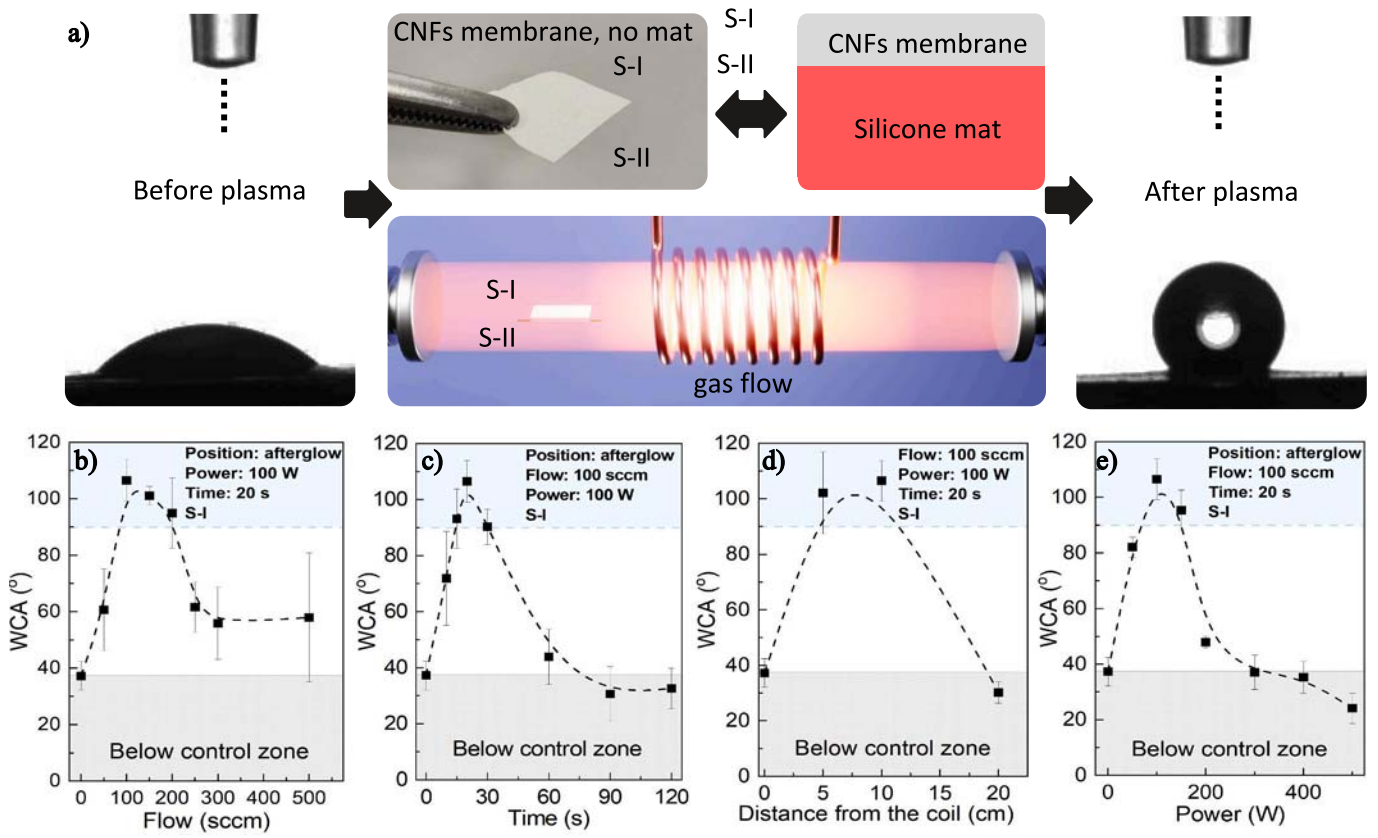

Fig. 1. a) Search for hydrophobicity of CNFs via nitrogen plasma processing with demonstration of WCA for the control and the sample with highest hydrophobicity, accompanied by detailed summary of the examined plasma parameters (b) nitrogen flow, c) treatment time, d) distance from the coil, e) plasma power) with respect to the WCA of S-I surface.

investigated by the means of scanning electron microscopy (SEM, Prisma E, Thermo Fischer Scientific), using the Everhart–Thornley detector (EDS, model Inca 400, Oxford Instruments). SEM micrographs were taken at the near vacuum conditions and at accelerating voltage 5 kV to minimize beam damage effects. For the investigation of fibril dimensions, 10 mg of 3 wt% CNFs were dispersed in 20 mL of deionized water and analyzed according to a previously described protocol (Oberlintner, Huš, et al., 2022).

Surface roughness was determined using AFM WITec Alpha 300 RA, employing force modulated tips (Force constant = 2.8 N/m and Resonance frequency 75 kHz) using tapping method. The measured area was 20 × 20 μm.

The composition of the CNF surface was analyzed by X-ray photoelectron spectroscopy (PHI-TFA XPS spectrometer from Physical Electronics Inc.). After treatment, the samples were placed on the sample holder and inserted in the ultra-high vacuum chamber with a pressure of no more than 10–8 Pa. The analyzed surface had a diameter of about 0.4 mm and the typical depth was not more than 5 nm. The surfaces were irradiated with X-rays with a photon energy of 1486.6 eV using a monochromatic Al source. The spectra were quantitatively analyzed using Multipack v8.1 software and fittings were conducted using the OriginLab software. The spectra were corrected with C1s at 284.8 eV.

Optical properties of CNFs-based membranes were evaluated with spectrophotometer UV-VIS Lambda 40P (Perkin Elmer, USA) in range of 800 to 200 nm with a step of 0.1 nm. The membranes were cut into rectangular pieces with dimensions 1 × 2 cm and leaned against the front of the cuvette. Opacity was calculated according to Eq. (1) (Han & Floros, 1997; Zhao et al., 2022):

$$Opacity = \frac{2 - log(T_{600})}{L} \quad (1)$$

where T_{600} is transmittance at 600 nm (%) and L is film thickness (mm). The measurements were done in triplicates with the average reported.

The thickness of the CNFs-based membranes was evaluated using Digital Micrometer (Mitutoyo, Japan). The measurements were carried out on at least 6 different points across the sample and the average is reported.

Tensile strength (σ) and elongation at break (ε) of the samples (2 × 6 cm) were evaluated at a crosshead speed of 25 mm min^{-1} using XLW Auto Tensile Tester (Labthink® Instruments, China), equipped with a 100 N load cell. The calculation of the parameters was carried out Lystem™ Lab Data Sharing System.

Lastly, water repellency was followed over the course of 21 days, measuring WCA every 7 days. During the aging process, the samples were stored at room temperature and at RH 50 %.

Thermal stability was evaluated through measurement of gravimetric change during exposure of the samples to temperatures in range between 40 °C and 800 °C with step of 10 °C under nitrogen with flow 20 mL min^{-1} using EGA 4000 (Perkin Elmer, USA). To analyze volatile products of deterioration, the cell was coupled with FTIR (Omega 3, Perkin Elmer, USA), scanning from 4000 to 400 cm^{-1} with resolution of 4 cm^{-1} with accumulation of 4 scans.

2.2.4. *Computational details*

Atomistic computations were performed at the density functional theory (DFT) level using the Gaussian 16 software. To allow for a correct description of the van der Waals interactions and account for charge transfer and polarization effects, a range-separated doubly hybridized functional wB97XD was used (Chai & Head-Gordon, 2008). Electron density was expanded in terms of 6-311++G(d,p), which is a large Pople's basis set including diffuse and polarization functions (Ditchfield et al., 1971). Free energies of solvation were calculated using a SMD

model (solvation model density) implementation of the polarizable continuum model (PCM) (Marenich et al., 2009), which is the preferred way when using implicit solvents.

As a compromise between the computational cost and chemical accuracy, cellulose was modelled using three monomeric (glucose) units. The ensuing cellotriose moiety was first geometrically optimized in the lowest-energy conformation without a solvent. Without further geometry optimization, the free energy of solvation was computed as the SMD is turned on. Effects of substituting the —OH group with —NH_2, —O—TMS (trimethylsilyl), —NHTMS and —N—$(TMS)_2$ on the free energy of solvation are then investigated and the electrostatic potential surfaces are drawn to visualize the differences.

3. Results and discussion

3.1. Wetting properties: in search of hydrophobicity

The main hydrophilicity/hydrophobicity indicator is the water contact angle (WCA) that was measured on the both sides of the sample immediately after the treatment. At first a search for hydrophobicity yielding conditions was conducted by treating top surface S-I of the membrane with low pressure inductively coupled nitrogen plasma, targeting the WCA > 90°, characteristic of hydrophobic surfaces. The parameters tested were power (0–500 W), flow (0–500 sccm), time (0–120 s), and finally the position of the sample inside the tube, examining center of the coil (0 cm), edge of the coil (5 cm), near afterglow (10 cm) and far afterglow (20 cm). After a such survey, resembling our previous experience with CF_4 plasma (Oberlintner, Shvalya, et al., 2022; Oberlintner, Vesel, et al., 2022), hydrophobicity pattern was obtained in multiple occasions with mild plasma treatment regime, determining the best water repellant performance at 100 W, 100 sccm, 20 s of plasma exposure in the near afterglow position (10 cm), reaching WCA of 106± 7° in average (Fig. 1b–d). Interestingly, after an optimal treatment, hydrophobic behavior is not seen for the S-II side of the CNFs-based membrane, as its WCA rises only slightly, from 37° to 45°, firmly remaining in the hydrophilic zone (WCA < 90°). Contrary to nitrogen, the oxygen plasma did not bring WCA of the S-I side over the control sample at any tested power, revealing a monotonous decrease from an initial 37° down to 15° (Fig. S2), confirming not only hydrophilic effect of oxygen plasma over CNFs-based membranes, but also crucial involvement of nitrogen plasma in hydrophobization.

Further on, the CNFs-based membrane was flipped upside-down, inserted into tube and treated at optimal nitrogen conditions (Fig. 2a). As opposed to the set-up ('S-I facing up' configuration) depicted in Fig. 1, the S-II surface was now facing towards the top of the tube and the S-I surface was facing the bottom ('S-I facing down' configuration). This was done in order to unveil a possible effect of the underlying substrate, that could influence the initial topology (roughness) or/and the chemical composition of the membrane. After several treatments, the side of the membrane that was in contact with a silicone mat during casting and drying (S-II) showed no hydrophobic features as the WCA value never exceeded 50°. The S-I surface achieved an average WCA of about 123± 3°, surpassing the hydrophobicity achieved in previous measurements by 17° (see Fig. 1). In general, the improvement in WCA after multiple cross-checks was in the range of 10–15 % when the S-I side was facing the bottom during plasma processing. Moreover, the impact of CNFs film

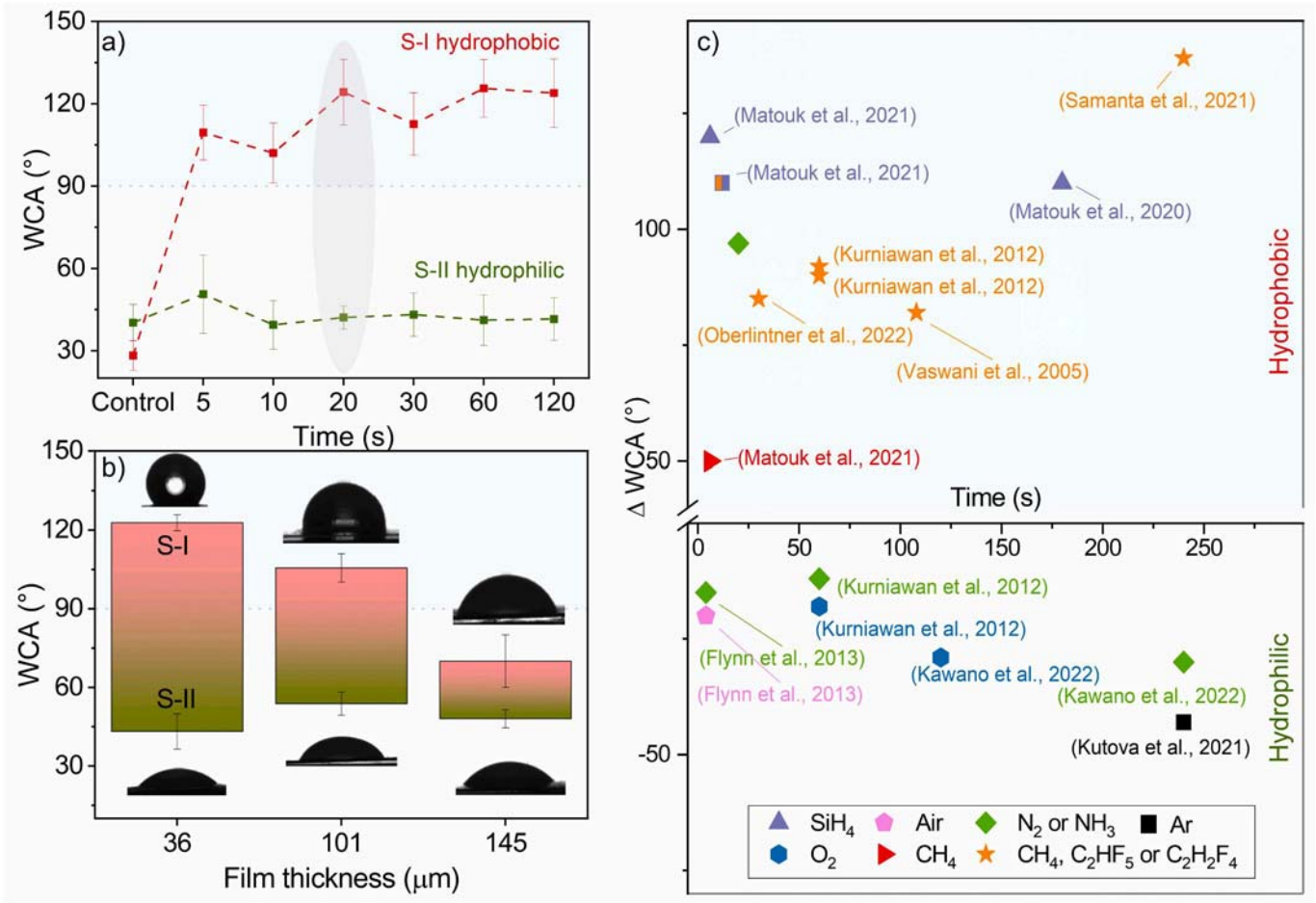

Fig. 2. a) Time-evolved WCA of the opposite sides S-I and S-II treated in the "S-I facing down" configuration. b) WCAs of CNFs-based membranes with various thickness. c) Placement of this study into the frame of existing literature utilizing plasma for change of wettability of cellulose nanomaterials.

thickness was tested using the latter treatment configuration as it revealed the best performance. Thus, to the existing 35 ± 2 μm sample two additional membranes with higher thickness 100 ± 6 μm and 150 ± 4 μm were fabricated. Synthesis of membranes thinner than 35 nm in profile was attempted, however, it was not possible to obtain a continuous coverage of silicone mat without cracking of CNFs membrane after drying. After the treatment it was evidenced that thinner membrane exhibits larger gap between hydrophobic S-I with WCA of 123± 3° and hydrophilic S-II (WCA 43 ± 6°) compared to thicker CNFs-based membranes (109 ± 5° for S-I and 54 ± 4° for S-II in membranes with medium thickness), and 70 ± 12° and 42 ± 6° for S-I and S-II, respectively, for the thickest fabricated membrane (Fig. 2b). The difference between wettability of the opposite sides decreases primarily due to lower hydrophobicity of S-I with increasing thickness, while wettability of S-II remains roughly the similar level.

The best performing case, namely, the thinnest CNFs-based membrane was put to test again, using time as a main parameter to observe. The WCA evolution was followed on both sides of the sample to have a better idea about the S-I surface in different treatment configurations ("S-I facing up" and "S-I facing down" configuration). Thus, by comparing WCA evolution through treatment time in Figs. 1d and 2a, it can be noted the "hydrophilic to hydrophobic switch" for S-I surface happens at the very beginning of the processing, as soon as in 5 s, reaches its maximum at about 20 s for both experiment configurations, and then starts to decline by entering a hydrophilic zone WCA < 90° for "S-I facing top" treatment, while staying hydrophobic for the configuration "S-I facing bottom" treatment till the end of treatment. The S-II side, on the other hand, has never experienced water-repellent performance. However, if both S-I and S-II considered together, it can be highlighted the membrane reveals now the dual wettability of the Janus character. Fig. 2c pinpoints the results of the present study into the frame of existing literature focusing on time spend to achieve a desired WCA features and highlights the rarity of hydrophobization through N_2 plasma approach. Such a unique WCA behavior of cellulose nanomaterial under environment friendly sustainable gas treatment observed in this study was never reported before, thus we took an opportunity to unveil the factors supporting these pioneering findings.

3.2. Surface morphology and topology: role of surface roughness

Typically, the solid surface-water interactions are controlled by topology or/and chemical features; thus, for Janus type behavior it might be expected their interplay is most likely a decisive. Firstly, the surface landscape of the control and treated specimen on both sides was inspected by SEM. CNFs-based membranes are composed of unordered fibrils with diameter of 14 ± 3 nm and length of few μm (11 ± 5.8 μm), as measured by the means of TEM (Fig. S1). It should be noted, that during drying at atmospheric pressure to obtain the membrane, the fibrils aggregate, therefore single fibril is not visible in SEM micrographs. However, the drying at 40 °C under atmospheric pressure was chosen in line with previous experience that led to formation of film that is prone to modification with plasma and exhibits appropriate mechanical and barrier properties (Lavrič et al., 2021; Oberlintner, Shvalya, et al., 2022). Comparison of the same side of the control sample to membrane treated at optimal plasma settings, namely "control S-I" vs "treated S-I" and "control S-II" vs "treated S-II", demonstrates no notable change, such as formation of pores or destruction of the surface to the fibers or aggregation. On the other hand, difference in the surface smoothness, created by casting the membranes onto the silicone substrate, resulting in S-II to be less structured and more flattened than S-I surface that is visible already by naked eye, and even better visualized with SEM (Fig. 3).

For further quantitative insight into topology of the samples and its role in the wetting behavior, AFM analysis was carried out to observe and evaluate the differences in the surface roughness. In general S-I exhibits average roughness (SA) of 937 ± 20 nm, while S-II with is twice as smooth with SA of 420 ± 20 nm. The difference between the topology of S-I and S-II can be observed by inspecting 2D (Fig. 4a) and 3D (Fig. 4b) profiles of CNFs-based membranes. It could be speculated that higher roughness (reader should note that the scale for "treated S-I" spans up to 1300 nm), is not caused by plasma, but is more likely is related to random fibril elevation over an average sample surface. When the initially hydrophilic surfaces (WCA for both about 37 ± 4°) were treated in a "S-I facing up configuration", the WCA increased to 106± 7° (S-I) and 43 ± 3° (S-II), indicating a large impact of surface roughness to water repellency. However, when the samples were treated in a "S-I facing down configuration", the measured WCA values were increased, reaching 123 ± 3° for S-I side and 54 ± 6° for S-II side. Considering that the surface with higher roughness results in lower wettability regardless of the experiment configuration, and that the hydrophobicity is not observed in the non-treated samples, the impact of morphology alone in not enough to induce hydrophobicity, but rather the Janus character is created through interplay of chemical change induced by plasma processing and different morphologies on the opposite sides. To obtain a full insight into the effect of plasma processing on the surface of CNFs-based membranes, composition study was performed.

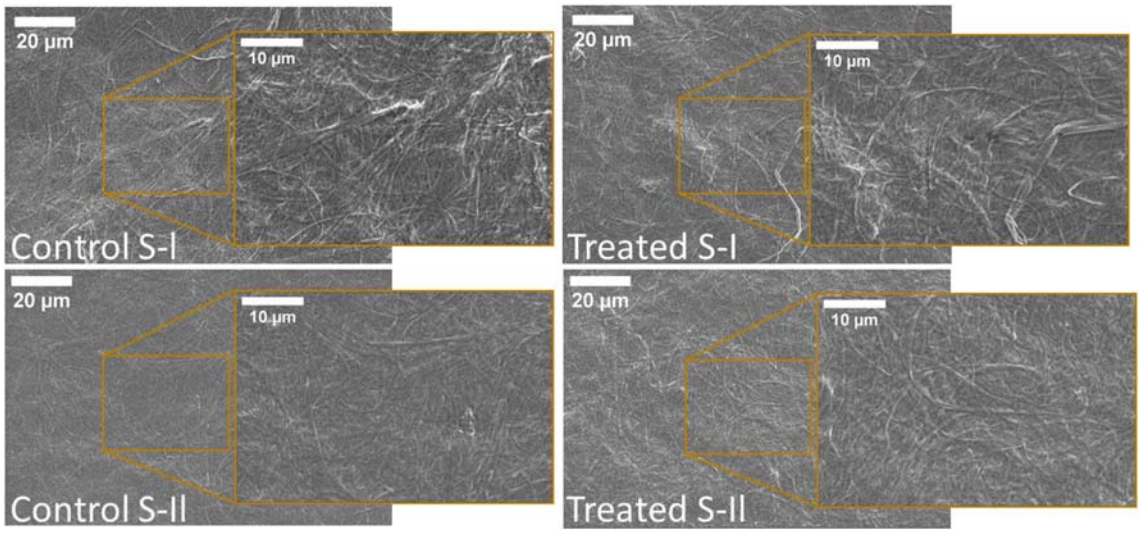

Fig. 3. Low and high magnification SEM micrographs of the S-I and S-II side for a control and S-I and S-II surfaces of the same membrane with Janus behavior after nitrogen plasma exposure.

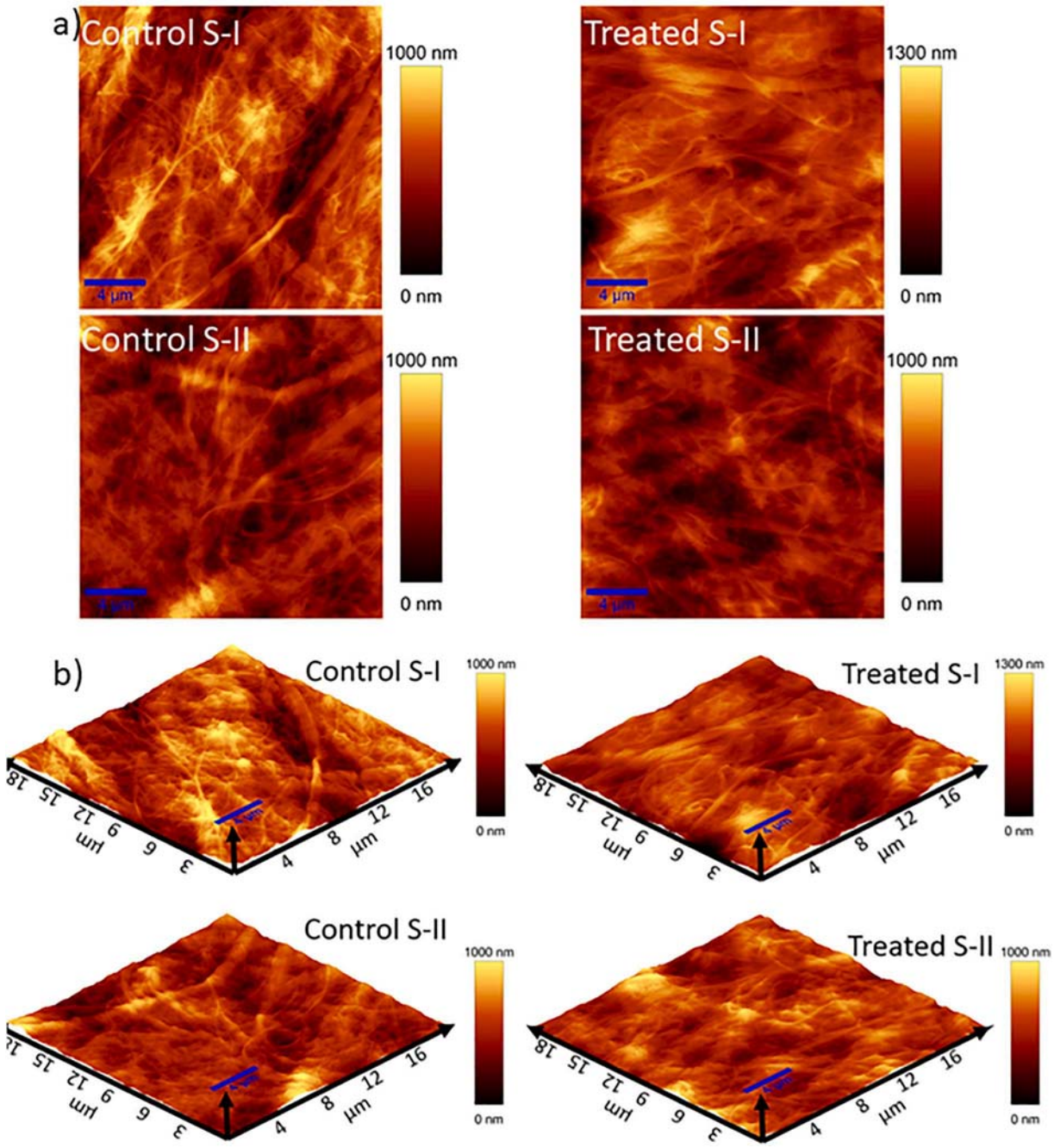

Fig. 4. AFM analyses of S-I and S-II of control CNFs-based membrane and treated samples with Janus behavior in a) 2D and b) 3D. The samples were treated in a "S-I facing down" configuration.

3.3. Surface chemistry behind the hydrophobicity of the CNFs-based membranes

Following the surface morphology inspection, the XPS was performed to unveil the consequences of nitrogen plasma treatment resulting in hydrophobicity. For clarity, XPS data will be discussed as following: (i) comparing two opposite sides of a control sample (same membrane, yet different morphology): (ii) surface with higher roughness (S-I of control sample) and plasma treated samples in different configurations (facing top versus facing bottom of the tube). By comparing survey spectra for "control S-I" and "control S-II" Si can be found in both cases with its content higher in S-II (5.6 at.% compared to 4.5 at.% in S-I, Table 1), which is the surface that was in a contact with the substrate during drying. Inspecting pure cellulose (nano)materials,

Table 1
Composition of the control samples on the opposite sides with different morphologies and calculated ratios between C/O, Si/O, and Si/C.

Sample	C1s (at. %)	O1s (at. %)	N1s (at. %)	Si2p (at.%)	C/O	Si/O	Si/C
Control S-I (rougher surface)	61.7	33.8	0	4.5	1.825	0.133	0.073
Control S-II (smoother surface)	59	35.3	0	5.7	1.671	0.161	0.097

dried directly on a Petri dish made of polystyrene, XPS reveals carbon and oxygen peaks solely, with no sign of Si, N or other major contaminants. Therefore, the only feasible reason for presence of Si (as seen in Table 2) is its leaching from the supporting silicone substrate to the CNFs membrane surface and its diffusion through the material. A general molecular structure of polysiloxanes, that leach from silicone materials (Horii & Kannan, 2008; Xu et al., 2017), consists of Si—O—Si backbone chain with framing groups (R), typically methyl (CH_3) groups and monofunctional siloxane unit. Polysiloxanes are known for their hydrophobic character, due to lack of polarity, and such material types are very welcomed in medical and food industry having a long track of success (Fortuniak et al., 2013; Ganicz & Rozga-Wijas, 2021). Recently polysiloxanes microspheres and coatings were used to improve hydrophobicity of paper material reaching WCA exceeding 100° (Pospiech et al., 2021). In this study, neither microparticles nor coatings were implemented, only plasma treatment of CNFs-based membrane doped with organosilicons. However, despite the presence of Si, both surfaces (S-I and S-II) are hydrophilic before subjecting them to plasma, meaning there is no yet chemical functionality between polysiloxanes and CNFs membrane to achieve its hydrophobicity.

After plasma exposure, only the rougher surface, S-I, became hydrophobic, exhibiting WCA of 106° in "S-I facing up" treatment and 123° in "S-I facing down" treatment configurations. Comparing the Control S-I to its treated version, it can be firmly stated nitrogen is found in both sample placement options, revealing higher content at the "S-I facing up" treatment configuration (Table 2). Notably the Si content has increased significantly after plasma processing, reaching 11 at.% in the latter and 20 at.% in sample S-I treated in "facing down" configuration. On the other hand, carbon and oxygen shares decreased in a opposite manner to Si with carbon seeing a larger drop compared to oxygen.

To unveil a possible hydrophobicity mechanism, the surface components were studied in detail. Following a discussion line of the sample side with higher roughness (S-I), the more indicative C1s core spectra were deconvoluted using Voight function. Contrary to a typical (nano) cellulose spectrum which is usually described by four distinct peaks ($C—C/C—H$ = 284.7 ± 0.1 eV, $C—O/C—OH$ = 286.6 ± 0.1 eV, $O—C—O$ = 287.9 ± 0.1 eV, and $O—C═O$ = 288.8 ± 0.1 eV) (Abdellah et al., 2018; Zhu et al., 2022), the control sample in this study was fitted with an additional component related to Si—C bonding, placed at 284.2 ± 0.1 eV (Fig. 5a). After plasma exposure in both configurations the C1s profile has changed drastically, new C—N component was introduced respectively to the nitrogen content observed, exhibiting higher peak for the "S-I facing top" geometry (Fig. 5b). From C1s deconvolution it can be suggested the fitted area of C—O/C—OH component is the one that changes the most with its huge reduction from 1.51 (Control S-I) to 1.1 and further to 0.37 in treated in "S-I facing up" and "S-I facing down", respectively. In turn, the Si-C component rises from 0.10 to 0.35 and finally to 0.45 following the same (sequence "control", "S-I facing up", and "S-II facing down") trend (Table 2). These C1s alteration might be related to a plasma facilitated substitution (C to Si, C—O to C—N and Si—C) and functionalization (Si—CH_3, C—NH_2) of CNFs surfaces with hydrophobic groups. The N1s fitting supports an appearance of C—N and amino (—NH_2) groups (Fig. 5c), however, considering a relative nitrogen share after treatment it might be said their contribution in hydrophobicity plays a secondary role in respect to possible Si—CH_3 functionalization. Further, no deconvolution was provided for O1s and Si2p, instead difference spectra were plotted ("Treated S-I facing up" subtracted from control in light red and the difference between control and "treated S-I facing down" in dark red in Fig. 5e), which provided a general but distinct insight for both chemical components. Thus, after applying C1s correction (C—C/C—H, 284.8 eV) it can be suggested (Fig. 5d, O1s) the removal of C—OH plays a significant role in hydrophobicity (positive values indicating control has higher content, while negative values mean higher content was detected in the treated sample). At the same time, treated surfaces are features with Si—O—C and Si—O—Si, which might be related to functionalization of a nanocellulose with polysiloxanes chains. Similar is observed while observing Si2p core level, treated samples are characterized by Si—O—C components (Fig. 5e, Si2p). Additionally, the "S-I facing down" configuration suggests there is still unfunctionalized Si—O—Si chain present in a control sample. Summarizing XPS observations, the following conclusions can be drawn: i) there is a trade-off between removal of OH and functionalization with Si—CH_3 (by the removal of OH groups the composition ratio of Si—CH_3 becomes higher) that is significant for hydrophobicity from chemical viewpoint; ii) C—N and —NH_2 are of secondary effect for hydrophobicity.

To further confirm findings obtained from XPS data, the structural properties were inspected by FTIR spectroscopy. The main confirmation of the proposed mechanism for hydrophobization would be the presence of Si—CH_3 features, comparing CNFs-membrane casted silicone substrate or directly on polystyrene petri dish, which remained hydrophilic on both sides after the plasma treatment (Table S1). Furthermore, on the newly obtained hydrophobic surface, the additional changes in C—O, C—N, C═O and more importantly O—H, N—H and C—H features would signal reorganizations in OH groups and presence of hydrophobic groups.

Table 2
Atomic composition of S-I in samples, with comparable topology, treated in "facing up" and "facing down" configuration, and calculated ratios between C/O, Si/O, and Si/C.

Sample	C1s (at. %)	O1s (at. %)	N1s (at. %)	Si2p (at. %)	C/O	Si/O	Si/C
Control S-I	61.7	33.8	0	4.5	1.825	0.133	0.073
Treated S-I (S-I facing up configuration)	51.1	33.3	4.4	11	1.525	0.328	0.215
Treated S-I (S-I facing down configuration)	45.8	31.8	2.4	20	1.44	0.629	0.437

3.4. Structural fingerprint via vibrational analysis

To observe functional changes induced by plasma processing and identify the reason behind newly obtained Janus behavior, ATR-FTIR analyses of control and treated sample were employed on both sides. All spectra feature characteristic peaks for cellulose (Fig. 6a): stretching vibrations between 3600 cm^{-1} and 3100 cm^{-1}, corresponding to intermolecular and intramolecular hydrogen bonds in the OH groups in cellulose I crystal, CH_2 symmetric and asymmetric stretching (centered at 2900 cm^{-1}), CH2 bending vibration of crystallinity band (1429 cm^{-1}), in-plane CH bending (1369 cm^{-1}), asymmetrical stretching of C—O—C glycosidic bond (1160 cm^{-1}) and C—C, C—OH and C—H ring and side group vibrations (1056 cm^{-1}) (Ci et al., 2024; Oh et al., 2005). It is important to note, that contrary to CNFs-based membranes fabricated without silicone substrate (polystyrene petri dish was used), both sides of the samples exhibit a slightly pronounced peak at 2961 cm^{-1} corresponding to CH_3 stretching vibrations, a strong peak centered at 1258 cm^{-1} that indicates presence of Si—CH_3 compounds, and peaks located at 860 cm^{-1} and 796 cm^{-1}, both attributed to bending of Si—CH_3 in polysiloxanes that migrated from the silicone substrate to the CNFs-based membrane (Fig. 6a). However, although exhibiting distinctive morphology, ATR-FTIR and XRD spectra S-I and S-II (Control S-I and control S-II in Figs. 6 and S4) do not indicate any structural difference between the opposite sides.

Upon treatment, changes are detected in six distinctive regions (Fig. 6b–f). Starting at the highest wavenumbers (3400 cm^{-1}–3100 cm^{-1}) in the region of O—H, a slight change after plasma processing is detected on both sides of the sample, pointing to either substitution of surface OH groups or to disruption in the initial intra and intermolecular hydrogen bonding with possible formation of N—H groups, especially

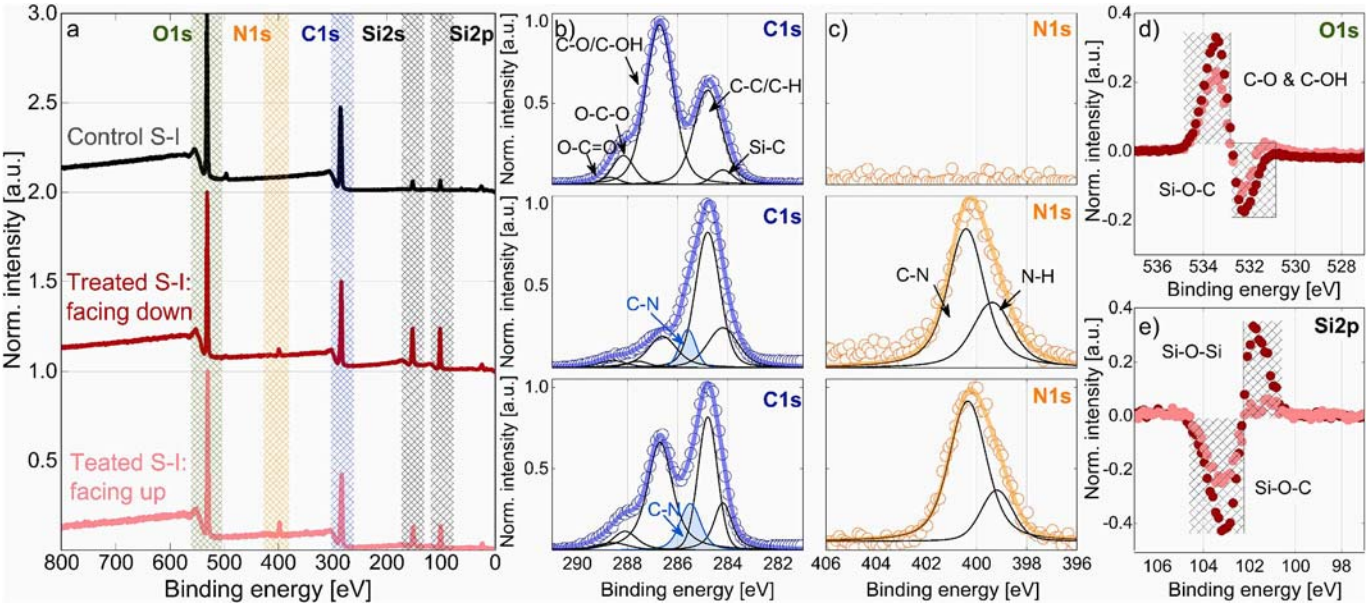

Fig. 5. a) Survey spectra for a control (black) and two treated samples in "Treated S-I facing up" and "Treated S-I facing down" configurations. b and c) The corresponding Shirley background corrected high resolution C1s and N1s core level spectra fitted with Voight profile. d and e) The differential spectra representing a deviation of the treated samples from a control. Dark red represents S-I treated "facing up" and a light red stand for a S-I treated "facing down" configuration.

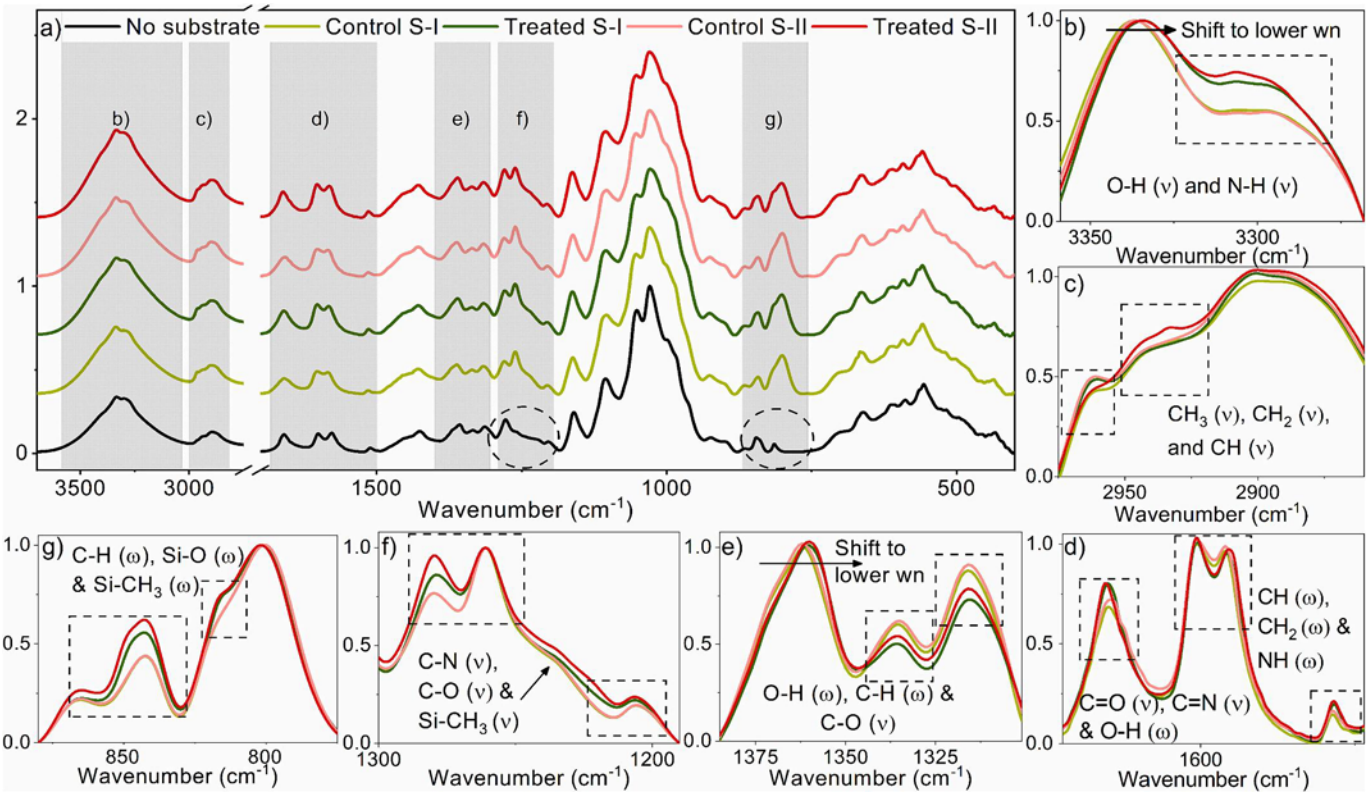

Fig. 6. a) ATR-FTIR spectra of the CNFs-based membrane casted without silicone substrate, S-I and S-II of control and treated samples, with marked and enlarged regions of interest after plasma processing (b–f).

while observing changes in a low-frequency part of the selected range. It should be noted, that at wavenumbers higher than 3340 cm^{-1} (Fig. 6a), is featured by steeper slopes for treated samples, indicating a partial removal of OH groups. Similarly, in a region attributed to —C—H stretching vibrations, a minor bump, that could be credited to CH_2 stretching, appears between 2955 cm^{-1} and 2920 cm^{-1}. Considering the structure of cellulose and taking in account that CH_2 functional group is present only at C6, change of the vibration spectra related to it, points to substitution at this position. In the region typical for stretching vibrations of double bonds (1700 cm^{-1}–1620 cm^{-1}), peaks related to C═O, possibly C═N stretching (which was not clearly evident from XPS data, due to components overlapping) and O—H bending vibrations of

adsorbed water on the surface overlap. However, comparing control and treated samples, the same trend is visible on both sides. The intensity of the peak centered at 1661 cm^{-1} increases after exposure to plasma indicating possible formation of C═N bonds. Similarly, peak located at 1582 cm^{-1} becomes more pronounced after plasma treatment, while also exhibiting a slight shift to lower wavenumbers on both hydrophobic and hydrophilic side. In the region of CH, CH_2 and NH bending, an increase in intensity is noted in the treated samples.

In domain of O—H bending vibrations (1375 cm^{-1}–1353 cm^{-1}), again, a slight shift to lower wavenumbers is observed in the treated sample on both sides. On the other hand, C—H and C—O related vibrations are weaker after the treatment. Between wavenumbers 1300 cm^{-1} and 1200 cm^{-1}, where C—O and C—N stretching deformations are featured, indicating possible formation of amine groups and changes in C—OH functional groups on cellulose ring. At the same time, Si—CH_3 related peaks (stretching vibrations between 1250 cm^{-1} and 1260 cm^{-1}, and bending vibrations between 865 cm^{-1} and 760 cm^{-1}) are increased in intensity after plasma processing. Similar peaks were detected in silicone substrate used for membrane formation signaling that leaching of silicon and methyl group via interface might be relevant for hydrophobic behavior.

3.5. Free energies of solvation

Generally, hydrophilic materials exhibit a favorable, strongly negative free energy of solvation. As hydrophobic groups are introduced to the material, the free energy of solvation, ΔG_{solv}, increases, rendering the process less likely. An overall free energy of solvation for a complex polymer is a function of its chemical composition and physical properties, such as porosity, shape, and interlinking. In this section, we are interested in the hydrophobic effect due to the chemical modifications, which is studied by systematically changing the most exposed (on the C^6) OH group. In Fig. 7, we plot in $\Delta\Delta G_{solv} = \Delta G_{solv(modified\ cellotriose)} - \Delta G_{solv(cellotriose)}$.

Two possible modifications were studied. First, treatment with nitrogen plasma can introduce surface —NH_2 groups (as seen in ATR-FTIR spectra in Fig. 6), which prove to be more hydrophobic than —OH. Substituting the C^6—OH group with —NH_2 increases the free energy of solvation for 1.7 kcal mol^{-1}, whereas a wholly hydrophobic substitution would bring about a + 5.6 kcal mol^{-1} increase (modelled as a —CH_3 substitution). Furthermore, in the reaction with siloxane, the —OH group is exchanged with —O—TMS, which increases ΔG_{solv} for 5.7 kcal mol^{-1}. A fully hydrophobic substitution of similar steric hindrance, approximated as —CH_2-*t*-butyl, increases ΔG_{solv} for 6.5 kcal mol^{-1}.

However, the ensuing —NH_2 groups from plasma treatment can also be modified by siloxanes, yielding —NH—TMS or —N—$(TMS)_2$ with TMS denoting $Si(CH_3)_3$, which increase ΔG_{solv} even more by 7.6 and 9.9 kcal mol^{-1}, respectively. These groups exhibit even higher $\Delta\Delta G_{solv}$ values than reference —CH_2-*t*-butyl and —CH-(*t*-butyl)$_2$ with 6.5 and 8.3 kcal mol^{-1}. Nitrogen-containing modifications are only possible upon using nitrogen plasma treatment. These structures along with the electrostatic potential are shown in Fig. 8.

Lastly, we show that introducing a siloxane monomer is sufficient to achieve maximum hydrophobicity and no improvement is gained when a longer oligomer is used. For —$(O—DMS)_n$—O—TMS, DMS denoting $Si(CH_3)_2$, the $\Delta\Delta G_{solv}$ does not change noticeably as *n* is increased. A similar trend of roughly constant $\Delta\Delta G_{solv}$ is observed when going from —$(N—(TMS)_2)$ to —N—(TMS)((DMS—O)$_n$—TMS). On the other hand, while the C^6-OH is most exposed and accessible, and thus first substituted, the gains in ΔG_{solv} are additive when multiple OH groups are exchanged. For a trisubstituted (with —O—TMS) monomeric unit of cellulose, an increase in $\Delta\Delta G_{solv}$ is three-fold (+14.9 kcal mol^{-1}). For an amine-linked trisubstitution (3× —N—$(TMS)_2$), we observe $\Delta\Delta G_{solv}$ = +24.1 kcal mol^{-1}, which is a 2.4-fold increase compared to the monosubstituted structure ($\Delta\Delta G_{solv}$ = +9.9 kcal mol^{-1}). Less-than-ideal additive effect is due to steric hinderance of the bulky —N-$(TMS)_2$ units on C^2 and C^3, which do not come fully in contact with the solvent but instead interact with each other.

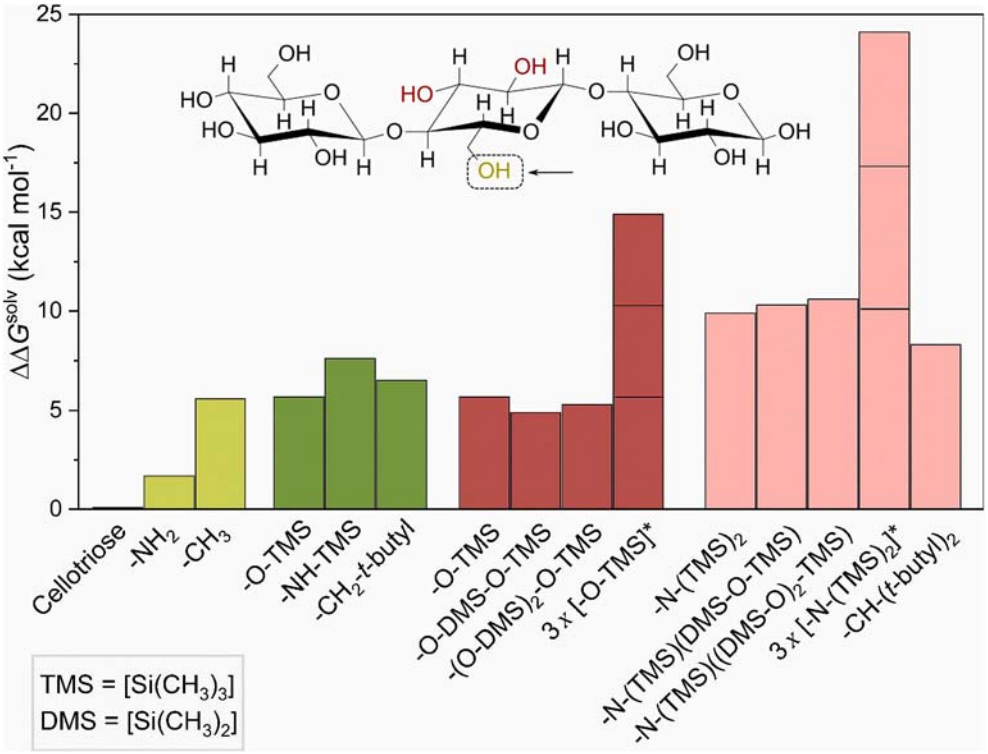

Fig. 7. Changes in free energy of solvation as the OH group on C^6 (circled) in cellotriose is substituted. A more positive value represents greater hydrophobicity. Various *t*-butyl substituents are used as model compounds for inert hydrophobic groups of comparable steric hindrance. Asterisk (*) denote that all three (C^2, C^3, C^6) OH groups are substituted, showing that the effect is additive.

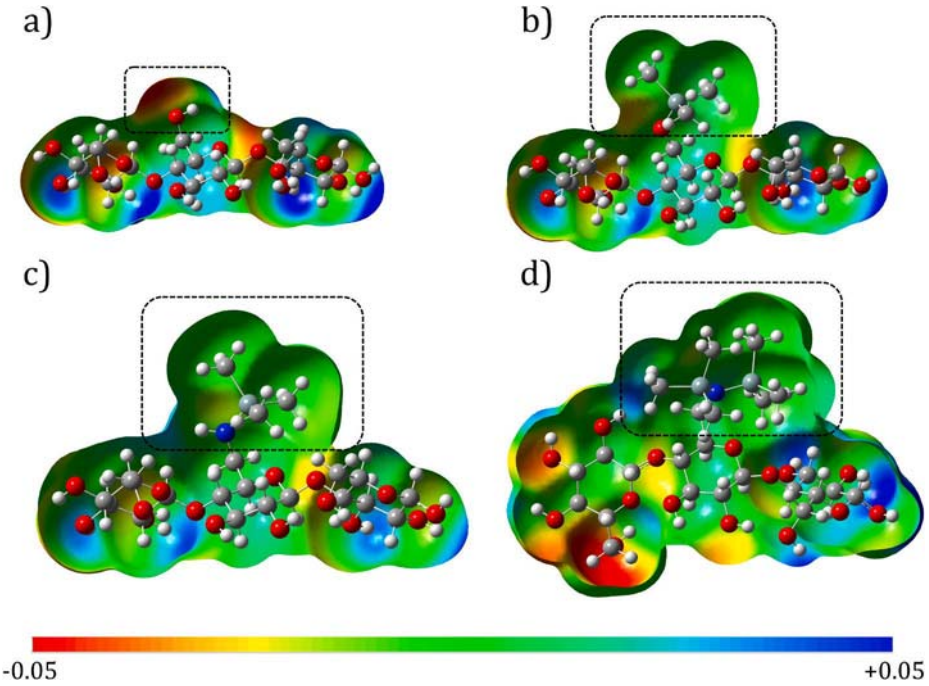

Fig. 8. Electrostatic potential (ESP) mapped on the total electronic density (95 %) for a) cellotriose and b) C_6—O—TMS, c) C_6—NH—TMS, and d) C_6—N—$(TMS)_2$ substitutions. Substitutions of the OH group decrease the absolute value of ESP in the dashed boxes, which effects greater hydrophobicity.

In real samples with a more complex structure, all modifications can and do occur, resulting in a mixture of —NH_2 < —O—TMS < —NH—TMS < —N—$(TMS)_2$, which introduce hydrophobicity in the ascending order. The latter two are *more* hydrophobic than model *t*-butyl groups, explaining the crucial effects of using nitrogen plasma.

4. CNFs-based Janus material for wound dressing applications

Lastly, physicochemical properties relevant for application, such as wound dressing were tested. For such purpose, the material should protect the skin from the environmental humidity and prevent it from coming into contact with skin, while at the same time absorbing the sweat or other bodily fluids. To demonstrate the ability of CNFs-based membranes with Janus character to fulfill these requirements, a drop of water, colored blue for better visibility, was deposited onto side II (the hydrophilic side), while pink colored-drop was deposited on the opposite side (side I) (Fig. 9a).

The produced CNFs-based materials were white in color and

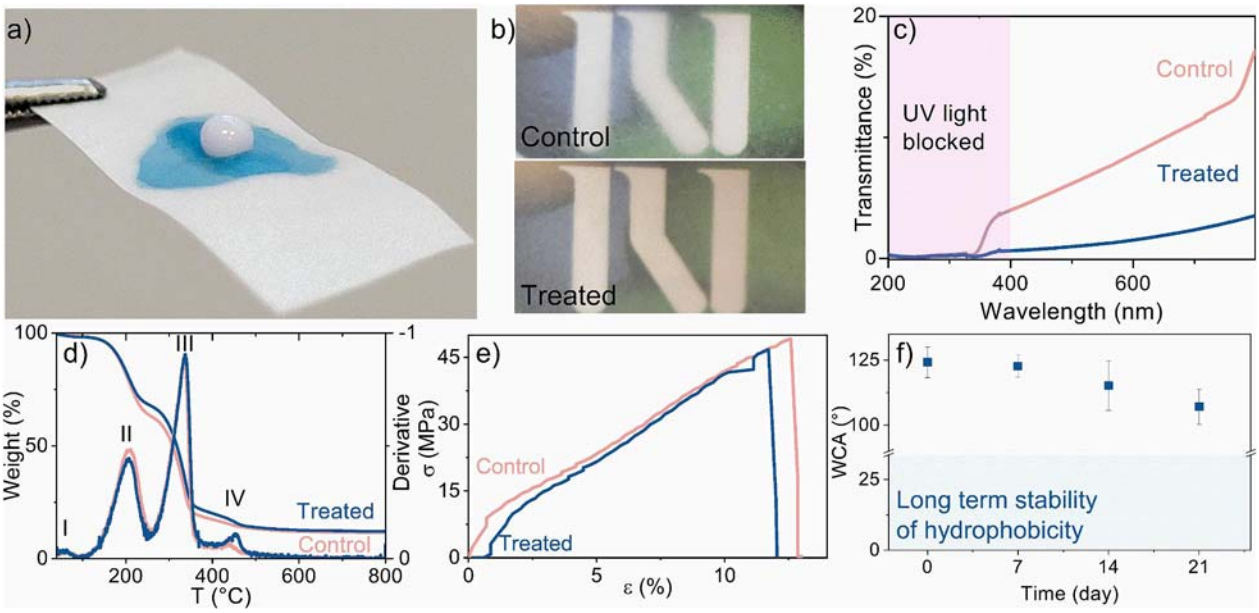

Fig. 9. a) The ability of the fabricated CNFs-based Janus material exhibits to absorb water on the hydrophilic side, while retaining hydrophobic character on the other. b) The produced membranes were white and translucent, with the treated sample exhibiting higher opacity and slightly beige shade.; c) Transmittance of control and treated samples. Both exhibit the ability to block UV light. d) Weight loss (left axis) and its first derivative (right axis) of CNFs-based materials during thermal degradation with labeled four distinctive stages. e) Stress-strain curve for control and material with Janus behavior. f) Stability of newly obtained hydrophobicity over the course of 21 days.

translucent. The untreated membranes were milky-white, that adopted a slightly darker shade of white, beige, upon plasma processing, as observable in Fig. 9b. In range of visible light (800 nm–400 nm), transmittance decreases relative to wavelength in both control and treated sample. However, the latter exhibits higher opacity (51 ± 6.4), with transmittance at 600 nm 1.5 % ± 0.8 %, compared to control with opacity of 30.0 ± 0.4 and transmittance at 600 nm 8.6 % ± 0.3 % (Fig. 9c). In the region of UV light, the membranes transmit virtually no light, exhibiting an excellent UV barrier. With final application for wound dressing in mind, this feature is of a great advantage, as the ability to block UV-light and thus protect the skin at sun exposure is crucial, due to its correlation to skin damage and pigmentation during wound healing (D'Orazio et al., 2013).

Thermal stability and degradation mechanism were observed employing TGA-FTIR, where volatile products that are the result of mass loss are analyzed. Both control and CNFs-based Janus materials degrade under elevated temperature in 4 distinct stages, as noted in Fig. 9d. The first stage (labeled I), with temperatures up to 100 °C involves dehydration or loss of unbound water (amounting to approx. 2 wt%) that is typical for biopolymers (D'Acierno et al., 2020). The next step of degradation (labeled II) occurs in range between 105 °C and 260 °C, where 45 % of initial weight is lost. The treated sample exhibits a slightly higher stability in this stage. Evolved gas analysis (Fig. S5) reveals formation of carbohydrate related compounds, such as CH_4, carboxylic acids, as well as CO, but does not detect CO_2 which is present in the third stage of degradation (III, 270 °C–370 °C). Finally, heating the sample beyond 420 °C causes the last (IV) stage of degradation where volatile products include R-CO-R′ that indicate degradation of the skeleton of cellulose (Shen & Gu, 2009). After being heated to 800 °C 12 % of the initial weight remains as solid waste in both control and treated sample.

Good mechanical strength and flexibility of the material are crucial for applicability of the produced Janus materials (Fig. 9e). TS was found to be 49 ± 1.9 MPa for control and 47 ± 3.1 MPa for plasma processed sample, indicating no change in mechanical strength upon treatment. The results are comparable to literature (Jaiswal et al., 2021). On the other hand, ε, was 13 ± 1.8 % and 12 ± 2.9 % for control and treated samples, respectively, which is slightly higher than described in the literature (Mokhena et al., 2021). This effect could take place as a result of addition of glycerol as a plasticizer into the film-forming dispersion. For practical applications long-term stability of the newly obtained hydrophobic properties is a crucial parameter, which was determined by following the WCA over the course of 21 days. A slight drop in WCA from the initial 124° to 115° was observed after aging the sample 14 days and to 107° after 21 days, however the surface still remained in the hydrophobic zone (Fig. 9f). This observation further points to high potential for utilization of the produced CNFs-based Janus membranes for medical textiles. Additionally, the exposure of the as-prepared materials to water droplet over the course of 3 min with continuous capture of WCA, revealing slow decline of WCA for approximately 3° per minute (Fig. S6a). Lastly, durability of the newly obtained hydrophobicity to abrasion with sandpaper was tested, showing resistance to abrasion up to 3 cycles (Fig. S6b). Further abrasion caused loss of hydrophobicity, however it should be noted that tearing of the membrane was also observed, leading to loss of physical properties as well.

5. Conclusions

This study presents a novel approach to fabrication of CNFs-based membranes with Janus behavior through exploitation of polysiloxanes and nitrogen plasma. Initial screening of plasma settings (plasma power, nitrogen flow, distance of the sample in from the coil, sample orientation and treatment time) determined optimal parameters at which WCA of S-I reached over 120°, while S-II remained hydrophilic (WCA of 45°). Detailed inspection of the surface morphology and chemistry, revealed mutual effect of surface roughness and composition on the final wettability. From chemical perspective, hydrophobization is mainly a result of simultaneous removal of OH and functionalization of CNFs with Si—CH_3, while newly formed nitrogen-related compounds are of lower influence. Substituting each —OH group with —NH_2 decreases the interaction with water by 1.7 kcal mol^{-1}, while introducing a O—Si$(CH_3)_3$ group decreases the interaction by 5.7 kcal mol^{-1}, making it fully hydrophobic (—CH_2—CH_3 and —CH_2-*t*-butyl) changes the free energy by 5.6 and 6.5 kcal mol^{-1}. Modifying —NH_2 groups with siloxanes yields —NH—Si$(CH_3)_3$ and —N(Si$(CH_3)_3)_2$, decreasing the interaction by 7.6 kcal mol^{-1} and 9.9 kcal mol^{-1}, respectively. In essence, introducing the —Si$(CH_3)_3$ through amine —N-linkages makes the structure more hydrophobic compared to introducing them through the —O-linkages in OH groups, explaining why nitrogen plasma outperforms other plasma carrier gases. Indicating applicability of the produced Janus materials, absorption of liquids on the hydrophilic side while retaining hydrophobicity on the other, opacity and UV light barrier, thermal stability, mechanical strength and flexibility, were demonstrated, rendering the materials suitable for wound dressing applications. The presented work might be a further advanced by studies on controlled release of active pharmaceutical ingredients from the fabricated material, or as a substrate for printed sensors, producing a smart wound dressing.

CRediT authorship contribution statement

Ana Oberlintner: Writing – review & editing, Writing – original draft, Visualization, Methodology, Investigation, Formal analysis, Data curation, Conceptualization. **Vasyl Shvalya:** Writing – review & editing, Visualization, Methodology, Investigation, Funding acquisition, Formal analysis, Data curation, Conceptualization. **Neelakandan M. Santhosh:** Writing – review & editing, Methodology, Investigation, Funding acquisition, Data curation. **Martin Košiček:** Writing – review & editing, Methodology, Investigation. **Ivan Jerman:** Writing – review & editing, Methodology, Investigation. **Matej Huš:** Writing – original draft, Visualization, Methodology, Investigation, Formal analysis, Data curation. **Uroš Novak:** Writing – review & editing, Supervision, Project administration, Funding acquisition. **Blaž Likozar:** Writing – review & editing, Supervision, Resources, Project administration, Funding acquisition.

Declaration of competing interest

The authors declare that they have no known competing financial interests or personal relationships that could have appeared to influence the work reported in this paper.

Data availability

Data will be made available on request.

Acknowledgements

The authors are thankful to Edi Kranjc for XRD measurements and to Vuk Martinović for help with experimental work.

Funding

This study was funded by Slovenian Research and Innovation Agency research core funding No. P2-0152, as well as Horizon Europe projects PROPLANET (GA 101091842), SSBD4CHEM (GA 101138475), REMEDIES (GA 101093964) and UPSTREAM (GA 101060876). V. S. appreciates ARIS-J2-4490 grant, obtained from the Slovenian Research and Innovation Agency (ARIS). N. M. S acknowledges the Slovenian Research and Innovation Agency (ARIS) for the postdoctoral project Z2-4467. M. H. is funded by infrastructure funding I0-0039, as well as projects funding J1-3020, and J2-4424. Computational resources were provided by the HPC RIVR consortium and EuroHPC JU through Vega at the Institute of Information Science, Maribor, Slovenia (project IDs

S24O01-04 and S24O01-21).

Appendix A. Supplementary data

Supplementary data to this article can be found online at https://doi.org/10.1016/j.carbpol.2024.122558.

References

Abdellah, M. H., Pérez-Manríquez, L., Puspasari, T., Scholes, C. A., Kentish, S. E., & Peinemann, K.-V. (2018). Effective Interfacially polymerized polyester solvent resistant Nanofiltration membrane from bioderived materials. *Advanced Sustainable Systems, 2*, Article 1800043. https://doi.org/10.1002/adsu.201800043

Abuhantash, F., Abuhasheesh, Y. H., Hegab, H. M., Aljundi, I. H., Al Marzooqi, F., & Hasan, S. W. (2023). Hydrophilic, oleophilic and switchable Janus mixed matrix membranes for oily wastewater treatment: A review. *Journal of Water Process Engineering, 56*, Article 104310. https://doi.org/10.1016/j.jwpe.2023.104310

Agaba, A., Marriam, I., Tebyetekerwa, M., & Yuanhao, W. (2021). Janus hybrid sustainable all-cellulose nanofiber sponge for oil-water separation. *International Journal of Biological Macromolecules, 185*, 997–1004. https://doi.org/10.1016/j.ijbiomac.2021.07.027

Cao, M., Ju, J., Li, K., Dou, S., Liu, K., & Jiang, L. (2014). Facile and large-scale fabrication of a cactus-inspired continuous fog collector. *Advanced Functional Materials, 24*, 3235–3240. https://doi.org/10.1002/adfm.201303661

Cassie, A. B. D., & Baxter, S. (1944). Wettability of porous surfaces. *Transactions of the Faraday Society, 40*, 546–551. https://doi.org/10.1039/TF9444000546

Chai, J.-D., & Head-Gordon, M. (2008). Long-range corrected hybrid density functionals with damped atom–atom dispersion corrections. *Physical Chemistry Chemical Physics, 10*, 6615–6620. https://doi.org/10.1039/B810189B

Cheng, H., Xiao, D., Tang, Y., Wang, B., Feng, X., Lu, M., … Sui, X. (2020). Sponges with Janus character from nanocellulose: Preparation and applications in the treatment of hemorrhagic wounds. *Advanced Healthcare Materials, 9*, Article 1901796. https://doi.org/10.1002/adhm.201901796

Chu, P. K., Chen, J. Y., Wang, L. P., & Huang, N. (2002). Plasma-surface modification of biomaterials. *Materials Science & Engineering R: Reports, 36*, 143–206. https://doi.org/10.1016/S0927-796X(02)00004-9

Ci, Y., Ma, Y., Chen, T., Li, F., & Tang, Y. (2024). Facile dissolution of cellulose by superbase-derived ionic liquid using organic solvents as co-solvents at mild temperatures. *Carbohydrate Polymers, 330*, Article 121836. https://doi.org/10.1016/j.carbpol.2024.121836

D'Acierno, F., Hamad, W. Y., Michal, C. A., & MacLachlan, M. J. (2020). Thermal degradation of cellulose filaments and nanocrystals. *Biomacromolecules, 21*, 3374–3386. https://doi.org/10.1021/acs.biomac.0c00805

Dai, B., Li, K., Shi, L., Wan, X., Liu, X., Zhang, F., … Wang, S. (2019). Bioinspired Janus textile with conical micropores for human body moisture and thermal management. *Advanced Materials, 31*, Article 1904113. https://doi.org/10.1002/adma.201904113

Dimitrakellis, P., & Gogolides, E. (2018). Hydrophobic and superhydrophobic surfaces fabricated using atmospheric pressure cold plasma technology: A review. *Advances in Colloid and Interface Science, 254*, 1–21. https://doi.org/10.1016/j.cis.2018.03.009

Ditchfield, R., Hehre, W. J., & Pople, J. A. (1971). Self-consistent molecular-orbital methods. IX. An extended Gaussian-type basis for molecular-orbital studies of organic molecules. *The Journal of Chemical Physics, 54*, 724–728. https://doi.org/10.1063/1.1674902

D'Orazio, J., Jarrett, S., Amaro-Ortiz, A., & Scott, T. (2013). UV radiation and the skin. *International Journal of Molecular Sciences, 14*, 12222–12248. https://doi.org/10.3390/ijms140612222

Fei, Y., Tan, Y., Deng, Y., Xia, P., Cheng, J., Wang, C., … Lu, L. (2022). In situ construction strategy for three-dimensional Janus cellulose aerogel with highly efficient oil–water separation performance: From hydrophobicity to asymmetric wettability. *Green Chemistry, 24*, 7074–7081. https://doi.org/10.1039/D2GC02275C

Flynn, C. N., Byrne, C. P., & Meenan, B. J. (2013). Surface modification of cellulose via atmospheric pressure plasma processing in air and ammonia–nitrogen gas. *Surface and Coatings Technology, Mechanical and Tribological Properties of Biomedical Coatings and Surface-modified Biomaterials, 233*, 108–118. https://doi.org/10.1016/j.surfcoat.2013.04.007

Fortuniak, W., Chojnowski, J., Slomkowski, S., Pospiech, P., & Kurjata, J. (2013). Route to hydrophilic, hydrophobic and functionalized cross-linked polysiloxane microspheres. *Polymer, 54*, 3156–3165. https://doi.org/10.1016/j.polymer.2013.04.017

Ganicz, T., & Rozga-Wijas, K. (2021). Siloxane-starch-based hydrophobic coating for multiple recyclable cellulosic materials. *Materials, 14*, 4977. https://doi.org/10.3390/ma14174977

Habibi, Y., & Lucia, L. A. (2012). Nanocelluloses: Emerging building blocks for renewable materials. *Polysaccharide Building Blocks: A Sustainable Approach to the Development of Renewable Biomaterials*, 105–125. https://doi.org/10.1002/9781118229484.ch3

Haji, A., & Naebe, M. (2020). Cleaner dyeing of textiles using plasma treatment and natural dyes: A review. *Journal of Cleaner Production, 265*, Article 121866. https://doi.org/10.1016/j.jclepro.2020.121866

Han, J. H., & Floros, J. D. (1997). Casting antimicrobial packaging films and measuring their physical properties and antimicrobial activity. *Journal of Plastic Film & Sheeting, 13*, 287–298. https://doi.org/10.1177/875608799701300405

Hegemann, D., Brunner, H., & Oehr, C. (2003). Plasma treatment of polymers for surface and adhesion improvement. *Nuclear Instruments and Methods in Physics Research Section B: Beam Interactions With Materials and Atoms, Ionizing Radiation and Polymers, 208*, 281–286. https://doi.org/10.1016/S0168-583X(03)00644-X

Horii, Y., & Kannan, K. (2008). Survey of organosilicone compounds, including cyclic and linear siloxanes, in personal-care and household products. *Archives of Environmental Contamination and Toxicology, 55*, 701–710. https://doi.org/10.1007/s00244-008-9172-z

Jaiswal, A. K., Kumar, V., Khakalo, A., Lahtinen, P., Solin, K., Pere, J., & Toivakka, M. (2021). Rheological behavior of high consistency enzymatically fibrillated cellulose suspensions. *Cellulose, 28*, 2087–2104. https://doi.org/10.1007/s10570-021-03688-y

Kawano, T., Wang, M.-J., & Andou, Y. (2022). Surface modification of a regenerated cellulose film using low-pressure plasma treatment with various reactive gases. *ACS Omega, 7*, 44085–44092. https://doi.org/10.1021/acsomega.2c05499

Koşak Söz, Ç., Trosien, S., & Biesalski, M. (2018). Superhydrophobic hybrid paper sheets with Janus-type wettability. *ACS Applied Materials & Interfaces, 10*, 37478–37488. https://doi.org/10.1021/acsami.8b12116

Kurniawan, H., Lai, J.-T., & Wang, M.-J. (2012). Biofunctionalized bacterial cellulose membranes by cold plasmas. *Cellulose, 19*, 1975–1988. https://doi.org/10.1007/s10570-012-9785-2

Kutová, A., Staňková, L., Vejvodová, K., Kvítek, O., Vokatá, B., Fajstavr, D., … Švorčík, V. (2021). Influence of drying method and argon plasma modification of bacterial nanocellulose on keratinocyte adhesion and growth. *Nanomaterials, 11*, 1916. https://doi.org/10.3390/nano11081916

Kwak, D., Lei, Y., & Maric, R. (2019). Ammonia gas sensors: A comprehensive review. *Talanta, 204*, 713–730. https://doi.org/10.1016/j.talanta.2019.06.034

Lavrič, G., Oberlintner, A., Filipova, I., Novak, U., Likozar, B., & Vrabič-Brodnjak, U. (2021). Functional nanocellulose, alginate and chitosan nanocomposites designed as active film packaging materials. *Polymers, 13*, 2523. https://doi.org/10.3390/polym13152523

Lejeune, M., Lacroix, L. M., Brétagnol, F., Valsesia, A., Colpo, P., & Rossi, F. (2006). Plasma-based processes for surface wettability modification. *Langmuir, 22*, 3057–3061. https://doi.org/10.1021/la052515f

Li, Q., Huang, M., Li, F., Ling, Z., Meng, Y., Chen, F., … Wang, S. (2024). Biomimetic stable cellulose based superhydrophobic Janus paper sheets engineered with industrial lignin residues/nano-silica for efficient oil-water separation. *Industrial Crops and Products, 207*, Article 117774. https://doi.org/10.1016/j.indcrop.2023.117774

Li, W., Wang, S., Wang, W., Qin, C., & Wu, M. (2019). Facile preparation of reactive hydrophobic cellulose nanofibril film for reducing water vapor permeability (WVP) in packaging applications. *Cellulose, 26*, 3271–3284. https://doi.org/10.1007/s10570-019-02270-x

Liston, E. M., Martinu, L., & Wertheimer, M. R. (1993). Plasma surface modification of polymers for improved adhesion: A critical review. *Journal of Adhesion Science and Technology, 7*, 1091–1127. https://doi.org/10.1163/156856193X00600

Lv, Y., Li, Q., Hou, Y., Wang, B., & Zhang, T. (2019). Facile preparation of an asymmetric wettability Janus cellulose membrane for switchable emulsions' separation and antibacterial property. *ACS Sustainable Chemistry & Engineering, 7*, 15002–15011. https://doi.org/10.1021/acssuschemeng.9b03450

Marenich, A. V., Cramer, C. J., & Truhlar, D. G. (2009). Universal solvation model based on solute electron density and on a continuum model of the solvent defined by the bulk dielectric constant and atomic surface tensions. *The Journal of Physical Chemistry. B, 113*, 6378–6396. https://doi.org/10.1021/jp810292n

Matouk, Z., Rincón, R., Torriss, B., Mirzaei, A., Margot, J., Dorris, A., Beck, S., Berry, R. M., & Chaker, M. (2021). Functionalization of cellulose nanocrystal powder by non-thermal atmospheric-pressure plasmas. *Cellulose, 28*, 6239–6252. https://doi.org/10.1007/s10570-021-03927-2

Matouk, Z., Torriss, B., Rincón, R., Dorris, A., Beck, S., Berry, R. M., & Chaker, M. (2020). Functionalization of cellulose nanocrystal films using non-thermal atmospheric–pressure plasmas. *Applied Surface Science, 511*, Article 145566. https://doi.org/10.1016/j.apsusc.2020.145566

Mokhena, T. C., Sadiku, E. R., Mochane, M. J., Ray, S. S., John, M. J., & Mtibe, A. (2021). Mechanical properties of cellulose nanofibril papers and their bionanocomposites: A review. *Carbohydrate Polymers, 273*, Article 118507. https://doi.org/10.1016/j.carbpol.2021.118507

Oberlintner, A., Huš, M., Likozar, B., & Novak, U. (2022). Multiscale study of functional acetylation of cellulose nanomaterials by design: Ab initio mechanisms and chemical reaction microkinetics. *ACS Sustainable Chemistry & Engineering*. https://doi.org/10.1021/acssuschemeng.2c04686

Oberlintner, A., Likozar, B., & Novak, U. (2021). Hydrophobic functionalization reactions of structured cellulose nanomaterials: Mechanisms, kinetics and in silico multi-scale models. *Carbohydrate Polymers, 259*, Article 117742. https://doi.org/10.1016/j.carbpol.2021.117742

Oberlintner, A., Shvalya, V., Vasudevan, A., Vengust, D., Likozar, B., Cvelbar, U., & Novak, U. (2022). Hydrophilic to hydrophobic: Ultrafast conversion of cellulose nanofibrils by cold plasma fluorination. *Applied Surface Science, 581*, Article 152276. https://doi.org/10.1016/j.apsusc.2021.152276

Oberlintner, A., Vesel, A., Naumoska, K., Likozar, B., & Novak, U. (2022). Permanent hydrophobic coating of chitosan/cellulose nanocrystals composite film by cold plasma processing. *Applied Surface Science, 597*, Article 153562. https://doi.org/10.1016/j.apsusc.2022.153562

Oh, S. Y., Yoo, D. I., Shin, Y., & Seo, G. (2005). FTIR analysis of cellulose treated with sodium hydroxide and carbon dioxide. *Carbohydrate Research, 340*, 417–428. https://doi.org/10.1016/j.carres.2004.11.027

Pertile, R. A. N., Andrade, F. K., Alves, C., & Gama, M. (2010). Surface modification of bacterial cellulose by nitrogen-containing plasma for improved interaction with

cells. *Carbohydrate Polymers, 82*, 692–698. https://doi.org/10.1016/j.carbpol.2010.05.037

Pospiech, P., Olejnik, K., Mizerska, U., & Zakrzewska, J. (2021). Influence of polysiloxane microspheres on hydrophobicity, structure and mechanical properties of paper materials. *Cellulose, 28*, 1687–1702. https://doi.org/10.1007/s10570-020-03613-9

Provin, A. P., dos Reis, V. O., Hilesheim, S. E., Bianchet, R. T., de Aguiar Dutra, A. R., & Cubas, A. L. V. (2021). Use of bacterial cellulose in the textile industry and the wettability challenge—A review. *Cellulose, 28*, 8255–8274. https://doi.org/10.1007/s10570-021-04059-3

Recek, N. (2019). Biocompatibility of plasma-treated polymeric implants. *Materials, 12*, 240. https://doi.org/10.3390/ma12020240

Shen, D. K., & Gu, S. (2009). The mechanism for thermal decomposition of cellulose and its main products. *Bioresource Technology, 100*, 6496–6504. https://doi.org/10.1016/j.biortech.2009.06.095

Silva, B. E.d. A., Menezes, A. J.d., Delgado, A. O., Cruz, N. C., & Rangel, E. C. (2016). *Modification of the wettability of nanocellulose films by SF6 plasma treatment* (Presented at the 15 Brazilian MRS meeting, Brazil).

Thomas, B., Raj, M. C., B, A. K., H, R. M., Joy, J., Moores, A., … Sanchez, C. (2018). Nanocellulose, a versatile green platform: From biosources to materials and their applications. *Chemical Reviews, 118*, 11575–11625. https://doi.org/10.1021/acs.chemrev.7b00627

Valence, S.d., Tille, J.-C., Chaabane, C., Gurny, R., Bochaton-Piallat, M.-L., Walpoth, B. H., & Möller, M. (2013). Plasma treatment for improving cell biocompatibility of a biodegradable polymer scaffold for vascular graft applications. *European Journal of Pharmaceutics and Biopharmaceutics, 85*, 78–86. https://doi.org/10.1016/j.ejpb.2013.06.012

Vaswani, S., Koskinen, J., & Hess, D. W. (2005). Surface modification of paper and cellulose by plasma-assisted deposition of fluorocarbon films. *Surface and Coating Technology, 195*, 121–129. https://doi.org/10.1016/j.surfcoat.2004.10.013

Wang, F., Zhao, X.-j., Wahid, F., Zhao, X.-q., Qin, X., Bai, H., … Jia, S. (2021). Sustainable, superhydrophobic membranes based on bacterial cellulose for gravity-driven oil/water separation. *Carbohydrate Polymers, 253*, Article 117220. https://doi.org/10.1016/j.carbpol.2020.117220

Wang, S., Liu, K., Yao, X., & Jiang, L. (2015). Bioinspired surfaces with superwettability: New insight on theory, design, and applications. *Chemical Reviews, 115*, 8230–8293. https://doi.org/10.1021/cr400083y

Wang, W., Lin, J., Cheng, J., Cui, Z., Si, J., Wang, Q., … Turng, L.-S. (2020). Dual super-amphiphilic modified cellulose acetate nanofiber membranes with highly efficient oil/water separation and excellent antifouling properties. *Journal of Hazardous Materials, 385*, Article 121582. https://doi.org/10.1016/j.jhazmat.2019.121582

Xu, L., Zhi, L., & Cai, Y. (2017). Methylsiloxanes in children silicone-containing products from China: Profiles, leaching, and children exposure. *Environment International, 101*, 165–172. https://doi.org/10.1016/j.envint.2017.01.022

Xu, Z., Fan, J., Tian, W., Ji, X., Cui, Y., Nan, Q., … Zhang, J. (2024). Cellulose-based pH-responsive Janus dressing with unidirectional moisture drainage for exudate management and diabetic wounds healing. *Advanced Functional Materials, 34*, Article 2307449. https://doi.org/10.1002/adfm.202307449

Yang, H.-C., Hou, J., Wan, L.-S., Chen, V., & Xu, Z.-K. (2016). Janus membranes with asymmetric wettability for fine bubble aeration. *Advanced Materials Interfaces, 3*, Article 1500774. https://doi.org/10.1002/admi.201500774

Yasuda, H., & Matsuzawa, Y. (2005). Economical advantages of low-pressure plasma polymerization coating. *Plasma Processes and Polymers, 2*, 507–512. https://doi.org/10.1002/ppap.200500002

Yue, X., Zhang, T., Yang, D., Qiu, F., & Li, Z. (2018). Janus ZnO-cellulose/MnO2 hybrid membranes with asymmetric wettability for highly-efficient emulsion separations. *Cellulose, 25*, 5951–5965. https://doi.org/10.1007/s10570-018-1996-8

Zhao, J., Wang, Y., & Liu, C. (2022). Film transparency and opacity measurements. *Food Analytical Methods, 15*, 2840–2846. https://doi.org/10.1007/s12161-022-02343-x

Zhou, H., Wang, H., Lin, T., & Niu, H. (2022). A novel Janus fabric with stable amphibious directional oil transport function. *Chemical Engineering Journal, 427*, Article 131936. https://doi.org/10.1016/j.cej.2021.131936

Zhu, Q., Wang, T., Sun, X., Wei, Y., Zhang, S., Wang, X., & Luo, L. (2022). Effects of fluorine-based modification on triboelectric properties of cellulose. *Polymers, 14*, 3536. https://doi.org/10.3390/polym14173536

Zhu, Y., Wang, D., Jiang, L., & Jin, J. (2014). Recent progress in developing advanced membranes for emulsified oil/water separation. *NPG Asia Materials, 6*, e101. https://doi.org/10.1038/am.2014.23